

## Measurements of electrical conductivity and the mean ionization state of nonideal aluminum plasmas

I. Krisch and H.-J. Kunze

*Institut für Experimentalphysik V, Ruhr-Universität Bochum, 44780 Bochum, Germany*

(Received 26 May 1998)

Thin pure aluminum wires which are rapidly vaporized in small glass capillaries by means of a short pulse current from an electrical discharge convert into a nonideal plasma near solid density. For a short period of time, the inner wall of the rigid glass capillary confines the homogeneous plasma until the induced pressure pulse disintegrates the capillary. During this part of the discharge, no instabilities occur, and the transient plasma covers a range of parameters according to the charge of the capacitors: the particle density ranges from 0.001 to 1.0 g/cm<sup>3</sup>, the temperature from 7000 to 24 000 K and the electron density from  $2.0 \times 10^{25}$  to  $3.0 \times 10^{26}$  m<sup>-3</sup>. Plasma conductivity was deduced by simply applying Ohm's law to the measured voltage drop across the wire and to the measured current through the wire. [S1063-651X(98)14411-2]

PACS number(s): 52.25.Fi, 52.25.Jm, 52.25.Qt, 72.15.-v

### I. INTRODUCTION

Traditional plasma research mainly restricts itself to investigations on ideal plasmas, whereas the interest in nonideal plasmas grew only during the past two decades. Only then did efficient computer become available, that allowed complex modeling of nonideal plasmas for theoretical description. Many problems are closely associated with creating nonideal plasmas in the laboratory, and with their investigation. New pioneering technologies based upon laser and particle beams, x-ray lasers, plasma light sources, and controlled fusion now advance researches. Nonideal plasmas also occur in nature, for example in the core of dwarf stars or giant gaseous planets like Jupiter [1], or in the core of a lightning stroke, and focus experimental and theoretical investigation.

If the ratio  $\Gamma$  of the mean potential energy to the mean kinetic energy is of order unity or larger, the plasma generally is characterized as nonideal or, synonymously, strongly coupled. Depending on temperature, either the Coulomb force, the polarization, or the van der Waals interatomic force dominates the interaction. Since the plasmas considered in the following have already changed from a liquid to a gaseous state, the interaction only consists of the long-range Coulomb force, so that the ion coupling constant [2,3]

$$\Gamma_{ii} = \frac{Z^2 e^2}{4\pi\epsilon_0 k T d_i} \approx 2.69 \times 10^{-5} \frac{Z^{23} \sqrt{d_i}}{T_i} \quad (1)$$

is given by the ion temperature  $T_i$  in K, and the ion density  $n_i$  in m<sup>-3</sup>, via the ion sphere radius  $d_i = \sqrt[3]{3/4\pi n_i}$ . Assuming a singly ionized plasma with identical temperatures for ions, electrons, and atoms, the difference diminishes between the ion-ion, electron-electron, and electron-ion coupling constant. Relating to the following measurements,  $\Gamma$  is used, therefore, without any index due to  $Z=1$ . Since the aluminum atoms are only singly ionized, there is no hierarchy between the different types of coupling. This condition limits any attempt at modeling the plasma in such a way that no interaction should be neglected, in case  $\Gamma$  exceeds unity. As

a result, this plasma regime represents the most complicated case forcing experimental investigations. For comparison with theoretical predictions, it is important to study the transport properties of these plasmas, e.g., the electrical conductivity, and to obtain the exact dependence on the plasma parameters. Any degeneration must not be taken into account, because the degeneration parameter

$$\Theta \approx \frac{h^2 \sqrt{n_e^3}}{8m_e k T} \approx 4.37 \times 10^{-15} \frac{\sqrt{n_e^3}}{T} \quad (2)$$

does not exceed unity.

In spite of the growing interest in strongly coupled plasmas, basic research is still in its infancy. A few experimental measurements face a few theoretical calculations in this borderland of plasma physics and physics of the solid state.

The electrophysical reaction of metals depends mainly on the state of the electrons. The conductivity varies over several orders of magnitude at the transition from a liquid to a gaseous state. Whereas the electrons could move almost freely in liquid metals, they are bound to atoms in the gaseous state. At the interface and before, where matter loses its metallic properties, with a reduction of the particle density, the ratio  $\Gamma$  is of order unity or greater.

Aluminum is widely used in technical applications and, for that reason, its conductivity is of considerable interest. In regard to technical applications, these results can help to understand electrode processes, especially the optimization or suppression of the ignition process. The conductivity correlates with the ignition voltage and therefore with the ignition behavior, so that this knowledge affords users a suitable manipulation of heavy current switches, wire fuses, and the ignition itself in gas lamps.

Reliable measurements compel the optimization of a flexible arrangement, which allows one to produce homogeneous plasmas in a wide range of densities and temperatures. Since there is no easy way to produce a stationary strongly coupled aluminum plasma, the wire discharge in a glass capillary becomes a practical solution for realizing conductivity measurements in the high density range. By vaporizing the wire inside the capillary, the Bochum facilities comply with the

requirement for a short, but suitable, period of time. Electron density, particle density, temperature, and conductivity can be derived sufficiently accurately during this time. Another possibility to produce nonideal plasmas is by laser driven shock waves which compress the solid [4].

Earlier measurements by DeSilva and Kunze reported in a previous paper deal with the experimental conductivity determination of nonideal copper plasmas which cover a wide range of coupling parameters [5]. Except for the conductivity, the plasma parameter electron temperature, particle density, and electron density were derived by a code which solves the equation of state by just inputting the electrical parameters, the wire and capillary radius. The particle density results from a shell model, first calculating the capillary compression and expansion in an iterative recursion, and then deriving the plasma volume. Additional measurements have been done in water surrounding the wire without a capillary [6], and recently this setup was also used to study the conductivity of aluminum [7].

Within the scope of this work, both the conductivity and the other plasma parameters are determined experimentally. This paper concentrates on the examination of strongly coupled aluminum plasmas obeying the local thermal equilibrium (LTE) regime. Since the plasma is optically thick in the visible region, DeSilva and Kunze encountered difficulties determining the temperature by means of spectroscopy. An arrangement of absorption spectroscopy now copes with this problem. In contrast to conventional methods, which merely detect radiation from the surface, this method allows one to judge the homogeneity of the plasma during the discharge, and to measure electron density and temperature at each section of the plasma.

## II. EXPERIMENT

In contrast to conventional wire discharges just aimed at phenomenological examinations or at technical applications, a number of conditions limit a reasonable determination of the conductivity in this way. Both instabilities and inhomogeneities in temperature and density make a reliable interpretation of an apparent conductivity impossible. In order to prevent instabilities or at least slow down their appearance or growth, a correct choice of circuit parameters is necessary, and the surrounding medium should suitably confine the discharge. Further, bad contact between wire and electrode not only tends to support misinterpretation of spectroscopic measurements, but also makes the cylindrical plasma shape uncertain due to early peripheral discharges.

As a matter of principle, the discharge should pass in the aperiodic limit without any current ringing at the end. Gas discharges should play a minor role, meanwhile, and most of the energy stored in the capacitors should enter the wire at the beginning.

The experimental arrangement consists of two capacitors connected in a parallel summing of  $3.86 \mu\text{F}$ . The capacitor bank is charged to at least 10 kV to ensure vaporization of the wire, and it is discharged by closing a low-inductive pressurized spark gap switch. Although the charge combined with the capacitance defines the stored energy, an increase of the voltage above 16 kV only provokes a small increase in the energy entering the wire. On the other hand, at the beginning it tends to make peripheral discharges easier due to a

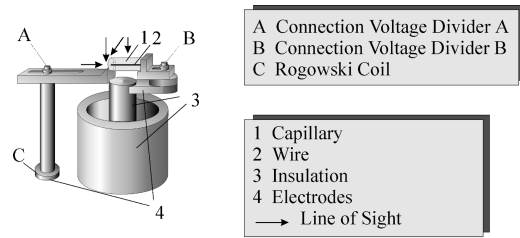


FIG. 1. Arrangement inside the discharge chamber.

higher radial electric field around the wire. A total inductance of 154 nH makes sure that the current can rise rapidly enough to avoid instabilities and prevent interaction between the wire and the peripheral medium. An extreme lowering of the inductance would impede a homogeneous deposition of energy.

For igniting the discharge, aluminum wires with 0.25 mm in diameter are passed through glass capillaries 22 mm in length, that have an inner diameter of 0.4 mm. The thickness of the wire guarantees a homogeneous vaporization without impairment due to skin effect. If the diameter is selected too small, the generation of peripheral discharges is supported due to a high electric field surrounding the wire at the beginning. The capillaries are clamped between two electrodes, as shown in Fig. 1.

After discharging the capacitors, Ohmic heating melts and then vaporizes the wire. The pressure in the capillary rises due to the rigid wall leading to a smooth transformation from the gaseous state into a nonideal plasma. Since the current density is sufficiently high, even the transition liquid-gaseous runs homogeneously [8]. The inner diameter of the capillary does not remain constant; see Fig. 2. The pressure pulse compresses the capillary wall, and it causes it to grow linearly with a velocity of  $5.1 \text{ mm}/\mu\text{s}$  ( $U_L = 16 \text{ kV}$ ), until the capillary splinters off and turns to dust. The higher the capacitor charge, the earlier the expansion of the inner diameter starts, and the faster it grows. During the discharge no instabilities occur, as shown in Fig. 3. Since there does not exist any phenomenon of reignition after a dark pause, the arrangement of inputting all energy right at the beginning is fulfilled well.

Suitable electrodes provided, the application of a capillary does not only improve the homogeneity of the plasma, but it also guarantees higher densities for a longer period of time.

Emission and absorption spectroscopic methods allow the deduction of electron density and temperature, even if the

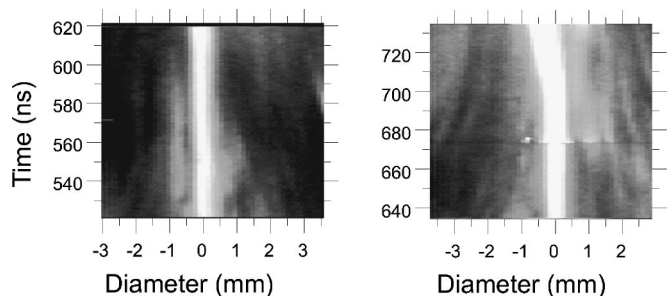


FIG. 2. Two typical streak photos of the plasma plume emanating from the end of the capillary taken side-on close to the capillary.

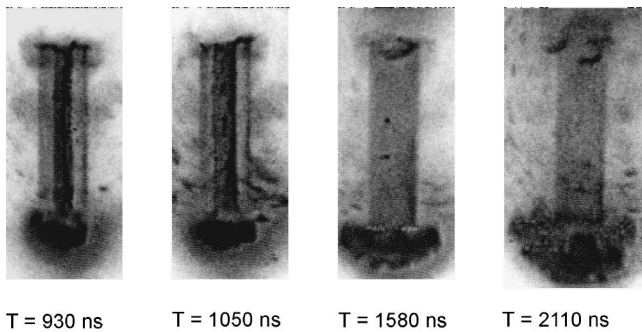


FIG. 3. Evolution of the discharge shown by CCD pictures.

encountered plasma is optically thick in the visible spectral range. All measurements are made by looking side on at the plasma plume which is exhausting at the ends. In order to attain conditions representative of the plasma within the capillary, the line of sight cannot cross the capillary walls, because scattering of radiation due to shivering makes a correct deduction impossible. Therefore, the point of observation was varied between 0.5 and 4 mm from the end of the capillary. The accurate plasma parameters then result from extrapolation into the capillary.

Different optical systems are used to detect and record the emitted electromagnetic radiation: (i)  $\frac{1}{8}$ -m monochromator and a 1-m monochromator equipped with an OMA system, (ii) two  $\frac{1}{4}$  monochromators each equipped with a photomultiplier, and (iii) a streak- and an ICCD camera to analyze the time development of the capillary. The current is calculated from the  $dI/dt$  signal of a Rogowski loop which surrounds the ground electrode, and the voltage drop across the plasma is determined by two voltage dividers; each divider is connected to one of the electrodes. Along the line of sight in the transverse direction, an additional light source backlights the exhausting aluminum plasma plume; see Fig. 4. This source is realized by a second plasma: a 12-ns ruby laser pulse of about 2 J ablates tungsten from a target positioned behind the capillary. Both plasmas cannot disturb each other; nevertheless their appropriate distance ensures intensive irradiance of the plume.

After entering the discharge chamber through a Brewster window, the laser light hits the target under an angle 78 (normal), because this concept ensures a good reproducibility of the backlighting plasma. Radiation emitted at 190 nm is used for the absorption measurement.

### III. SPECTROSCOPIC MEASUREMENTS FOR THE EVALUATION OF PLASMA PARAMETERS

While the emission of cosmic plasmas which become optically thick with respect to continuum radiation roughly ap-

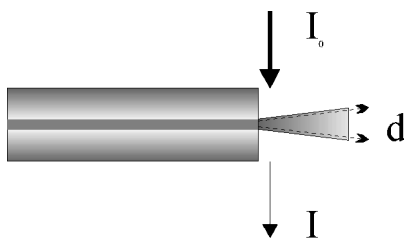


FIG. 4. Schematic view of the backlighting arrangement.

proach that of a blackbody, this similarity reduces to a limited spectral range concerning laboratory plasmas. At the beginning of the discharge, when converting the wire into a plasma, the emitted spectrum consists of continuous bremsstrahlung exclusively. If homogeneity and LTE are assumed and the optical depth  $\tau(\lambda, t)$  towers above 4, the spectral radiation reaches the Planck curve except for a deviation of 2% [9]. With respect to the aluminum plasma, this condition is fulfilled for  $\lambda > 420$  nm during the early period of the discharge. Later, the  $\tau(\lambda, t) > 4$  limit moves to longer wavelengths. A line spectrum consisting of emission and absorption lines of the species Al I to Al III superimposes the continuum beyond this limit. Except for the resonance lines, the plasma becomes optically thin, relating to both line and continuum radiation below 220 nm (proven by comparison of line intensities with the same higher level).

During the relevant period of the discharge, neither the sputtered electrode material nor the surrounding air disturb the aluminum spectrum or substantially pollute the plasma. As a result, evacuation of the discharge chamber yields no advantage.

Since the plasma is transient, the validity of LTE requires checking relevant time constants and estimating the electron collisional rates by the electron density [10]. The aluminum plasma is sufficiently dense and long lived. Electrons whose velocity distribution comes close to Maxwellian during the observed period of the discharge redress the balance. Four methods were used for the determination of the temperature in order to eliminate all doubts about this serious problem and to cover each relevant period of the discharge with data points.

(i) Provided that the plasma is optically thick, the temperature can be determined continuously by comparing the spectral radiance to a standard radiation source. Observing at 650 nm ensures that no line radiation distorts the signal.

(ii) In a second procedure, a Planck curve could be fitted to the spectrum and yielded the temperature. The gate time of the detection was 25 ns.

(iii) Approximately 1200 ns after the start, the superimposed line spectrum was recorded in the optical thin region ranging from 180 to 400 nm. The temperature was derived from the ratio of two different lines from the same ionization stage [11].

(iv) The Kirchoff-Planck function, depending only on temperature, describes the ratio of emission and absorption. Establishing a background plasma, the absorption was measured at roughly 190 nm, and it was compared to the emission calibrated absolutely [9].

Apart from typical deviations of 20%, all methods yield corresponding results; see Fig. 5(a). Only the effort is different. Figure 5(b) shows an example of the electron temperature measured at various distances from the end of the capillary. Close to the capillary it does not vary much, and thus justifies reliable extrapolation into the capillary.

The fourth method allows a precise description of the radial temperature dependence if optical alignment and imaging are correct. The plasma remains rather homogeneous for quite a long time; see Fig. 5(c). After 2  $\mu$ s, its temperature in the core is higher than that at the sheath.

A relation from Finckelnburg and Maecker for steady discharges [12],

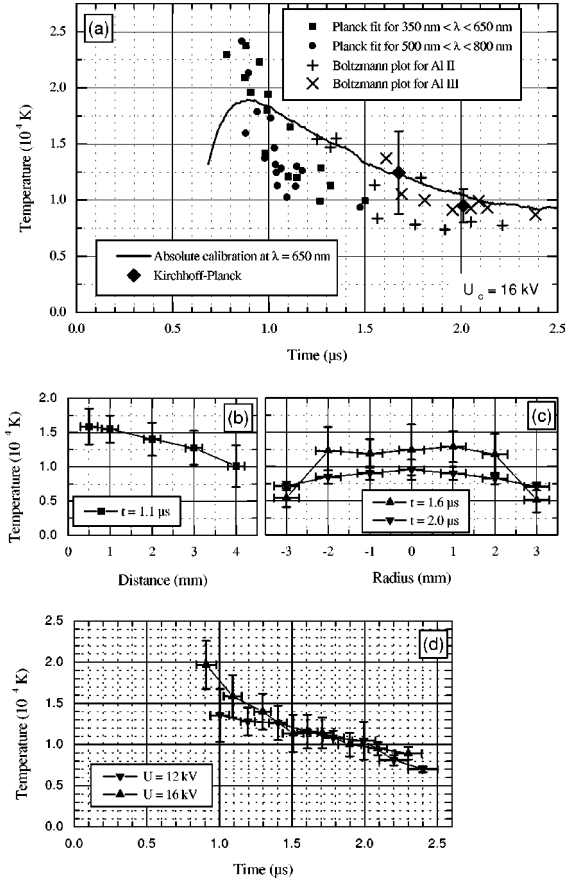


FIG. 5. Determination of the temperature. (a) Comparison of the temperature from all methods at a charge voltage of  $U_L = 16$  kV. (b) Extrapolation inside the capillary along the  $z$  axis of the plasma plume. (c) Radially resolved presentation. (d) Average of all methods at two different capacitor charge voltages.

$$\frac{T_e - T_g}{T_e} = \frac{m_{Al}}{m_e} \left( \frac{\lambda_e \varepsilon_0 E}{3kT_e} \right)^2, \quad (3)$$

helps to estimate the difference between electron temperature  $T_e$  and gas temperature  $T_g$  by inputting the mass ratio of aluminum ions  $m_{Al}$  and electrons  $m_e$ , the electric field  $E$ , and the mean free path length  $\lambda_e$  for electrons.  $\lambda_e$  results from the conductivity measurements. Already after 800 ns the deviation becomes less than 0.017.

The electron density  $n_e$  was estimated first by measuring the full width at half maximum  $w$  of different Al lines. The estimation employed scaled data from the literature for the interpretation using the isolated line approximation [13]. However, the results were completely unsatisfactory and scattered by two orders of magnitude. Therefore, they were discarded.

In order to obtain the accurate electron density, the backlighting technique has been used. Because the observed wavelength is below the cutoff and the plasma is without considerable magnetic field, the decrease of radiance  $L$  follows the general Lambert-Beer absorption law

$$dL(\omega, \vec{x}) = -k_{\text{total}}(\omega, \vec{x})L(\omega, \vec{x})d\vec{x} \quad (4)$$

in case the light passes the plasma. Since Rayleigh and Thomson scattering have an infinitely small share and line

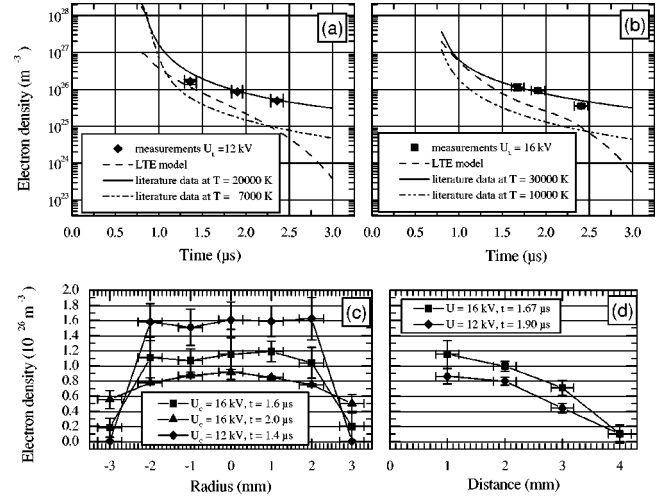


FIG. 6. Determination of the electron density. (a) Final results employing the backlighting technique. (b) Comparison between backlighting data just outside the capillary, LTE model, and data from literature [16]. (c) Radially resolved presentation. (d) Extrapolation into the capillary along the  $z$  axis of the plasma plume.

absorption does not exist due to suitable choice of wavelength, the absorption coefficient  $k_{\text{total}}$  only consists of the continuous absorption  $k_c(\omega, \vec{x})$ . The process of photoionization is negligibly small, as well. Although the aluminum plasma is nonideal and therefore correlation forces appear, the best and advantageous solution for a description originates in the quasiclassical approximation of Kramers and Unsöld [14]. The Gaunt factor  $\bar{G}(\lambda, T_e)$  includes the correlation effects [15], and ranges from 0.7 and 0.9 according to ionic charge. Using the Kirchhoff-Planck function because of LTE, the equation

$$k_{ff}(\lambda, T_e) = 1.3695 \times 10^{-27} \frac{n_e n_i Z^2 \lambda^3}{\sqrt{T_e}} \times \left( 1 - \exp \left\{ -1.4387 \times 10^{-2} \frac{1}{\lambda T_e} \right\} \right) \bar{G}(\lambda, T_e) \quad (5)$$

represents the absorption coefficient;  $k_{ff}$ ,  $\lambda$ , and  $T_e$  are given in m<sup>-1</sup>, m, and K, respectively, and the number value infers from calculated physical constants. Since the contribution of doubly ionized aluminum atoms does not exceed 5% compared to the entire ion density—as can be simply shown by means of the Saha-Eggert equation and the data of Drawin and Felenbok [16]—the electron density  $n_e$  can be equated with the ion density  $n_i$ . The ionic charge  $Z$  is derived by a code.

The final results are shown in Figs. 6(a) and 6(b) for two charging voltages. Also, this technique does not yield the density at early times because the plasma is optically thick. The measured electron density is also compared to a code (LTE model [16]) and to data given in the literature [17]. The code simply uses the Saha-Eggert equation, the measured temperature, and the lowering of the ionization poten-

tial due to static shielding. Since the plasma is optically thick at the beginning, the code gives an idea how the electron density then behaves.

Figure 6(c) illustrates the radial electron density distribution after Abel inversion; it remains homogeneous until later times of the discharge. In contrast to standard wire discharges, the radial spread occurs later. This certainly supports the use of a capillary as a surrounding medium to achieve a higher accuracy of the conductivity measurements. Figure 6(d) shows the density along the axis, and thus justifies the extrapolation of the results inside the capillary as a sensible method which increases precision. If the distance is increased to 4 mm and more, this method will lose its reliability there due to turbulences inside the plasma plume, leading to strong deviations.

#### IV. CONDUCTIVITY MEASUREMENTS

External forces, temperature, and density gradients affect the macroscopic transport of the energy and electric charge. Conversely, they accelerate the charged particles and destroy the thermal equilibrium and scattering processes, and diffusion redress the balance. The electrical conductivity  $\sigma$  describes the current density  $j$  resulting from an electric field. If magnetic fields can be neglected, the plasma will become isotropic, and the conductivity  $\sigma$  will be a scalar quantity. In general, the electrical conductivity

$$\sigma = en_e \mu_e \quad (6)$$

of a plasma is defined by the electron density  $n_e$  and the electron mobility  $\mu_e$ .

Here, the contribution of the ions has no effect on  $\sigma$ . Theoretical investigations are not able to characterize precisely the electron mobility  $\mu_e$  in the border case between liquid and the ideal plasma, because additional processes interact contrarily and therefore complicate the problem (e.g., polarization, static and dynamic shielding, electron degeneration and Pauli blocking, pressure ionization, interference of many particle scattering, and ion correlation) [18]. Only the two limiting cases, the degenerated electron gas in a metallic solid and the homogeneous ideal plasma, obey a simple description.

The time dependent development of the plasma resistance is derived by measuring the voltage drop across the plasma and the current flow through the plasma. The voltage consists of a resistive and an inductive component:

$$U = IR + \frac{d}{dt}(LI). \quad (7)$$

At the beginning of the discharge, the inductive component becomes important. Later, when electron density, temperature, and conductivity are determined, the resistive component dominates the voltage. Since the change in inductance due to the phase transition is negligibly small, solving for the plasma resistance  $R$  yields

$$R = \frac{U - LI}{I}. \quad (8)$$

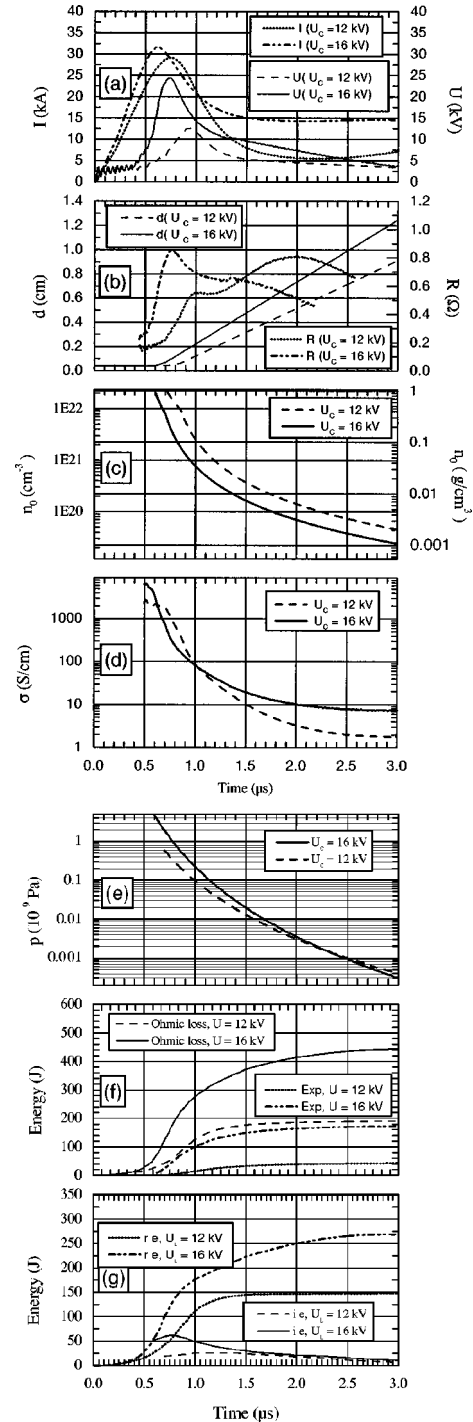


FIG. 7. Time record of two typical discharges containing (a) voltage and current; (b) diameter and resistance; (c) particle density; (d) conductivity; (e) pressure (SESAME); (f) Ohmic heating and expansion; and (g) the internal energy (ie) obtained from Ref. [17], and the reduced energy (re), which is the difference between the Ohmic heating and the expansion [both shown in (f)].

The conductivity of the plasma cylinder with cross section  $A(t)$  and length  $\ell$  can be written as

$$\sigma = \frac{1}{\rho} \quad \text{and} \quad \rho = R \frac{A(t)}{\ell} = R \frac{\pi r^2(t)}{\ell}. \quad (9)$$

In contrast to the length of the plasma column which remains

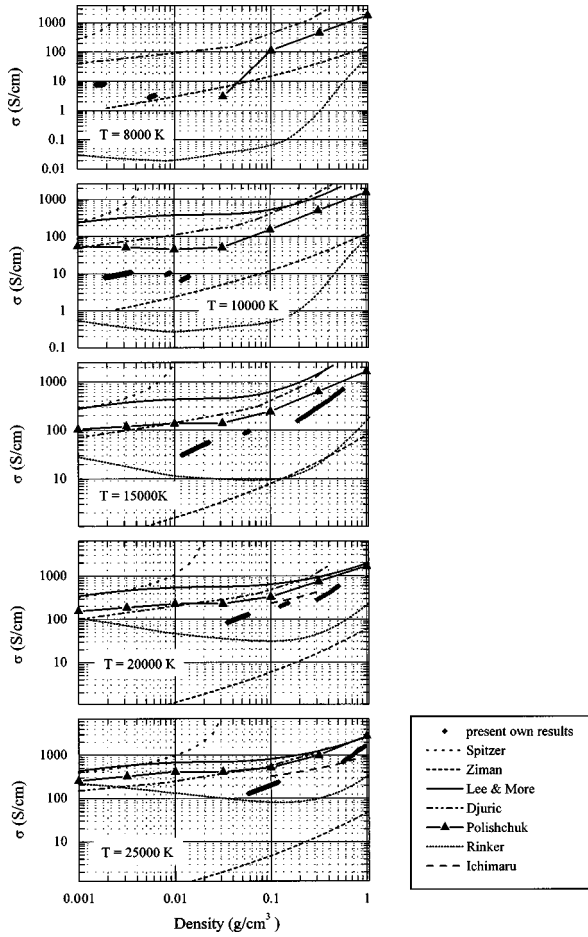


FIG. 8. Measured conductivity at different temperatures. Also shown are available theoretical results from Refs. [19], [20], [21], [22], [26], [23], and [24]. (a)  $T=8000$  K. (b)  $T=10\,000$  K. (c)  $T=15\,000$  K. (d)  $T=20\,000$  K. (e)  $T=25\,000$  K.

constant at  $\ell=22$  mm, its inner radius  $r(t)$  expands during the discharge, as shown in Fig. 7(e).

Before the expanding wire, whose start diameter is smaller than the inner diameter of the capillary, really fills in the capillary, there exists a slight uncertainty concerning the cross section  $A(t)$ . Figure 7 presents all important data referring to the discharge, and also focuses attention on different capacitor charges. The pressure curve in Fig. 7(g) originates from the SESAME code using the temperature and particle density as input parameters. If the internal energy derived by the SESAME code is compared to the reduced energy [Ohmic heating minus expansion of the wire, both shown in Fig. 7(h)], there appears an amazing difference; see Fig. 7(i). A correct energy balance must consider further losses such as shock waves in the surrounding capillary, the heating of the capillary, radiation losses, etc.

Both the voltage and the current behave as expected; see Figs. 7(a) and 7(b). The higher the capacitor charge, the more energy enters the wire and the more strongly the temperature increases. The wire vaporizes completely at the current maximum, and it converts from a conductor to an insulator. Since the number density of charge carriers is similar at the transition point for each capacitor charge, the absolute values of the current maxima do not differ much. After vaporization, the current and Ohmic heating decrease. The tem-

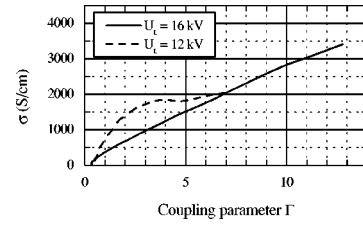


FIG. 9. Measured conductivity plotted as a function of coupling parameter  $\Gamma$ .

perature drops because of plasma expansion. As long as the capillary surrounds the plasma, its diameter increases almost linearly without any indication of instabilities. In spite of this behavior before splintering off ( $t>5.0\ \mu\text{s}$  for  $U_L=12$  kV, and  $t>3.9\ \mu\text{s}$  for  $U_L=10$  kV), the period of examination ends earlier due to inhomogeneities in electron density and temperature; see Figs. 5(c) and 6(c).

After vaporization the conductivity decreases monotonically more than two orders of magnitude during the period of investigation. Later, at  $T\approx 8000$  K, the conductivity changes less significantly owing to a weaker dependence on particle density. The ionization grows slightly. Altogether, the standard deviation is fairly small from shot to shot, so that all data can be reproduced very well. Even a few shots allow reliable measurements of the conductivity.

Without doubt, the conductivity does not depend on the electric field which results from the capacitor charge. Following an estimation relating to hydrogen [19] and assuming an electron density of  $n_e>2.0\times 10^{27}\ \text{m}^{-3}$ , a field of  $1.01\times 10^6$  V/m does not effect the conductivity.

## V. RESULTS

Figure 8 displays measured and theoretical data as function of particle density at different temperatures.

(i) If the temperature exceeds  $15\,000$  K, the conductivity increases monotonically with density.

(ii) For temperatures  $T\leq 10\,000$  K, the conductivity behaves nonmonotonically. Against the normal trend, the conductivity decreases between  $0.01$  and  $0.001\ \text{g/cm}^3$ . The lower the temperature, the more pronounced this tendency appears.

For the purpose of illustration and integration, Fig. 8 includes the results of the conventional Spitzer theory [20] and a simplified Ziman theory [21]. The Spitzer theory for ideal plasmas yields an upper limit in the density range  $0.01\ \text{g/cm}^3$ , and the Ziman theory representing the solid state regime yields a lower limit in the range between  $0.5$  and  $1.0\ \text{g/cm}^3$ . The Spitzer data follow from the assumption  $Z=1$  and from the input of measured electron density and temperature. The Ziman data are based upon a functional relation [21]

$$\sigma_e = \frac{n_e e^2 \Lambda_e}{m_e v_F}, \quad (10)$$

which merely includes scattering of the electrons at the thermal oscillations of the metal grid. It simply approximates the conductivity of a free electron gas by taking into account the mean free path length  $\Lambda_e$  of an electron and the Fermi velocity  $v_F$  which itself depends on the measured electron den-

sity. The mean free path length  $\Lambda_e$  is calculated by just using the Lindemann's melting law. This calculation neglects all interaction between the ions and their interference. However, it considers the neighbored ion as a geometric obstacle.

All results, Figs. 8(a)–8(e) support the hypothesis that available conductivity models are not sufficient for a wide range of description. Since modeling raises serious difficulties in the range of nonideal plasmas, measurements and experimental determination play an important role and are essential. Several models [22–25] describe quite well either the tendency of the conductivity curve, like the data of Bespalov and Polishchuk [26], or the correct order of magnitude, but always in a limited range of parameters. Neither the Ziman theory nor the Spitzer theory can yield a suitable solution in this range of parameters.

Similar to nonideal copper plasmas [5], the measured conductivity rises with increasing coupling  $\Gamma$ , as shown in Fig. 9. However, the results differ from each other for different discharges with different plasma parameter combinations. It thus becomes evident that the conductivity cannot be characterized just by the coupling parameter in the weakly nonideal range. Both the electron density and temperature are needed for a correct classification. This is also emphasized by Fig. 9, where the dashed line for 12-kV charging voltage corresponds to lower temperatures than the 16-kV case.

Finally, since electron and particle densities are known well, the data also allow a detailed discussion of the mean ionization state of the singly ionized aluminum plasma. The ionization strongly influences the conductivity values. Figure 10 shows a comparison between measured and literature data [17,24]. In particular, the SESAME data, based upon the Rinker model, predict a mean ionization that is too small. Perhaps this difference explains why the theoretical conductivity values of the Rinker code itself remain inaccurate. The results quoted in Ref. [17] are not based upon the SESAME data.

## VI. CONCLUSION

The Bochum facility, a modified wire arrangement, facilitates producing a nonideal aluminum plasma which obeys

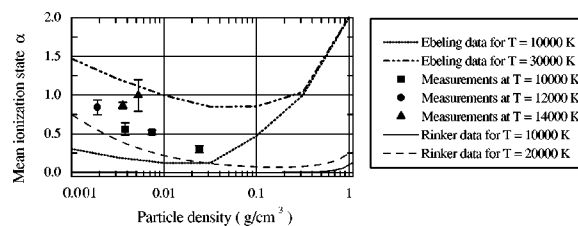


FIG. 10. Measured mean ionization state plotted as a function of particle density, and comparison to literature data [17,24].

LTE. Its homogeneity and its stability are guaranteed by a special choice of circuit parameters, and this is proven by backlighting spectroscopy and CCD pictures. The surrounding capillary supports this intention by extending the relevant period of possible measurements. In contrast to the preceding work by DeSilva and Kunze [5], all plasma parameters are determined experimentally by means of spectroscopy and electric detection. Here models just serve the purpose of comparison. Since the conductivity is well known as a function of various plasma parameters, these results promote an evaluation of existing theoretical models. Summing up, all considered models fail in a correct description over a wide range. Fundamental understanding forces experimental investigations.

Future plans focus on a detailed analysis of the transition from a conductor to an insulator. Further spectroscopic investigations will be extended into the vacuum ultraviolet range in order to examine closely the density range of pressure ionization and the transition to thermal ionization. At last, the correlation between both transitions can be checked.

## ACKNOWLEDGMENTS

We are indebted to Dr. S. Lyon for assistance in obtaining the relevant LANL SESAME tables. We greatly appreciate discussions with A. W. DeSilva.

- 
- [1] S. L. Shapiro and S. A. L. Teukolski, *Black Holes, White Dwarfs and Neutron Stars* (Wiley, New York, 1983).
  - [2] V. E. Fortov and I. T. Iakubov, *Physics of Nonideal Plasmas* (Hemisphere, New York, 1989).
  - [3] S. Ichimaru, H. Iyetomi, and S. Tanaka, *Phys. Rep.* **149**, 91 (1987).
  - [4] Th. Löwer and R. Sigel, *Contrib. Plasma Phys.* **33**, 355 (1993); T. Aoki, S. Hüller, and J. Meyer-ter-Vehn, *ibid.* **33**, 553 (1993).
  - [5] A. W. DeSilva and H.-J. Kunze, in *Physics of Nonideal Plasmas*, edited by W. Ebeling, A. Förster, and R. Radtke (Teubner-Texte, Leipzig, 1992), p. 200; A. W. DeSilva and H.-J. Kunze, *Phys. Rev. E* **49**, 4448 (1994).
  - [6] A. W. DeSilva, in *Proceedings of the International Conference on the Physics of Strongly Coupled Plasmas*, edited by W. D. Kraeft and M. Schlanges (World Scientific, Singapore, 1996).
  - [7] A. W. DeSilva and J. D. Katsouras, *Phys. Rev. E* **57**, 5945 (1998).
  - [8] A. D. Rakhel (unpublished).
  - [9] J. Richter, in *Plasma Diagnostics*, edited by W. Lochte-Holtgeven (North-Holland, Amsterdam, 1968), pp. 1–65; H. Zwicker, in *Plasma Diagnostics, ibid.*, pp. 214–251.
  - [10] H. R. Griem, *Principles of Plasma Spectroscopy* (Cambridge University Press, Cambridge, 1997).
  - [11] W. Lochte-Holtgeven, in *Plasma Diagnostics* (Ref. [9]), pp. 135–213.
  - [12] W. Finckelnburg and H. Maecker, in *Handbuch der Physik* (Springer-Verlag, Berlin, 1956), Vol. XXII.
  - [13] H. R. Griem, *Spectral Line Broadening by Plasma* (Academic, New York, 1974); M. Baranger, *Phys. Rev.* **111**, 481 (1958); **111**, 494 (1958); **111**, 855 (1958); G. Traving, in *Plasma Diagnostics* (Ref. [9]), pp. 66–134.
  - [14] A. Unsöld, *Physik der Sternatmosphären* (Springer, Berlin, 1955).
  - [15] W. J. Karzas and R. Latter, *Astrophys. J., Suppl.* **6**, 167 (1961).

- [16] H.-W. Drawin and P. Felenbok, *Data for Plasmas in LTE* (Gauthiers-Villars, Paris, 1965).
- [17] W. Ebeling, A. Förster, V. E. Fortov, V. K. Grryaznov, and A. Y. Polishchuk, *Thermophysical Properties of Hot Dense Plasmas* (Teubner-Texte, Stuttgart, 1991).
- [18] G. Röpke, Phys. Rev. A **38**, 3001 (1988); C.-V. Meister and G. Röpke, Ann. Phys. (Leipzig) **39**, 133 (1982).
- [19] K. Morawetz, M. Schlanges, and D. Kremp, Phys. Rev. E **48**, 2980 (1993).
- [20] L. Spitzer, *Physics of Fully Ionized Gases* (Wiley, New York, 1962).
- [21] J. M. Ziman, *Principles of the Theory Of Solids* (Cambridge University Press, London, 1972).
- [22] Y. T. Lee and R. M. Moore, Phys. Fluids **27**, 1273 (1984).
- [23] Z. Djuric, A. A. Mihajlov, V. A. Natasyuk, M. Popovic, and I. M. Tkachenko, Phys. Lett. A **155**, 415 (1991).
- [24] G. A. Rinker, Phys. Rev. B **31**, 4207 (1985); **37**, 1284 (1988); SESAME. The Los Alamos National Laboratory Equation of State Database. LA-UR-92-3407.
- [25] S. Ichimaru, S. Mitake, S. Tanaka, and X.-Z. Yan, Phys. Rev. A **32**, 1768 (1985); S. Mitake, S. Tanaka, X.-Z. Yan, and S. Ichimaru, *ibid.* **32**, 1775 (1985); S. Tanaka, S. Mitake, X.-Z. Yan, and S. Ichimaru, *ibid.* **32**, 1779 (1985); X.-Z. Yan, S. Tanaka, S. Mitake, and S. Ichimaru, *ibid.* **32**, 1785 (1985); S. Ichimaru and S. Tanaka, *ibid.* **32**, 1790 (1985).
- [26] I. M. Bespalalov and A. Ya. Polishchuk (unpublished). Data are tabulated in Ref. [17].